Journal of Materials Chemistry A

ROYAL SOCIETY OF CHEMISTRY

PAPER

View Article Online
View Journal | View Issue

Check for updates

Cite this: *J. Mater. Chem. A*, 2023, **11**, 6886

Effect of terminations on the hydrogen evolution reaction mechanism on Ti_3C_2 MXene†

Ling Meng, [ab] Li-Kai Yan, [*b] Francesc Viñes [*a] and Francesc Illas [a]

Two-dimensional (2D) MXene materials are proposed as high-efficiency hydrogen evolution reaction (HER) electrocatalysts. Most computational studies addressed the HER assuming a fully O-termination, even if as-synthesized MXenes feature a mixture of –O, –OH, –F, or even –H surface groups. To better understand the electrocatalytic surface composition and mechanism under HER equilibrium conditions in the Ti_3C_2 MXene model material, we composed Pourbaix diagrams considering *ca.* 450 topologically different surface terminations, including pristine Ti_3C_2, full –O, –OH, –F, and –H terminations, and binary and ternary situations with different group ratios. Realistic models built from Pourbaix diagrams near HER equilibrium conditions of low pH and *U* were used to investigate the Volmer–Heyrovsky and Volmer–Tafel mechanisms, with the particularity of considering, or not, the participation of H atoms from –OH or –H termination groups at different reaction stages. Results pointed out that the models close to the HER equilibrium line, $O_{2/3}OH_{1/3}$, $F_{1/3}O_{1/3}OH_{1/3}$, and $F_{3/9}O_{4/9}OH_{2/9}$, require an almost negligible overpotential of 0.01 V, while surface charges explain the impact of higher ratios of –O groups on modulating the H bond, and the positive influence of having surface –F groups.

Received 14th January 2023
Accepted 26th February 2023

DOI: 10.1039/d3ta00261f

rsc.li/materials-a

1. Introduction

The long-term problem of reaching a sustainable future by using clean and renewable energy sources has remained unsolved. A prospective candidate, hydrogen (H_2), has attracted great attraction as a possible clean and renewable energy source thanks to its high energy density and non-polluting properties when used as fuel,[1,2] especially when it is obtained from a renewable source such as wind and solar energy. The hydrogen thus obtained is usually referred to as *green* hydrogen to differentiate from that obtained from methane steam reforming, so far the most used source. When electricity can be obtained from these renewable sources, the electrocatalytic water reduction becomes a highly appealing way of producing H_2,[3,4] and here high-performing electrocatalysts are key to maximize the efficiency of the hydrogen evolution reaction (HER) process. Hitherto, Pt has been the most efficient electrocatalyst for the HER,[5,6] although its intrinsic HER activity is limited by mass-transport.[7] Moreover, the scarcity and high cost of Pt hinder its applications for large-scale electrocatalytic hydrogen production, and, therefore, the development of non-precious, Earth-abundant HER electrocatalysts, with high activities is essential to make the field move forward.

Recently, great research endeavors have been placed at meeting this goal by exploring non-precious metal substitutes such as Ni or Ni-based alloys.[8,9] However, while Ni is widely commercially used as a HER electrocatalyst, it is naturally unstable in acidic solutions, similar to other electrocatalysts used for the HER. Beyond Ni, various promising noble metal free two-dimensional (2D) materials with high activity towards the HER were proposed, including molybdenum dichalcogenides (MoS_2),[10–12] metal phosphides,[13] g-C_3N_4,[14–16] and graphene-based compounds.[17] However, one crucial weakness of these 2D catalysts is that they often exhibit a semiconducting nature, and have poor charge transfer properties.[10] Even if 1T-MoS_2 overcomes this handicap by being a relatively good conductor, it has been found to be unstable under ambient conditions.[12] Another drawback is that the catalytically active sites are normally restricted to edge or defective atoms, whilst most in-plane atoms are catalytically inert,[18] reducing the overall atomic efficiency and performance of the electrocatalyst. Therefore, a constant search for new stable 2D HER electrocatalysts with good charge transfer kinetics while displaying multiple, regular catalytic active sites is of utmost importance.

It is just in this aspect that MXenes have attracted great attention as electrocatalysts for the HER. MXenes are 2D transition metal carbide, nitride, or carbonitride materials with the general chemical formula of $M_{n+1}X_nT_x$, where normally $n = 1$–3, M is an early transition metal, and X = C and/or N.[19] The most-extended MXene synthesis involves the selective etching

[a]*Departament de Ciència de Materials i Química Física & Institut de Química Teòrica i Computacional (IQTCUB), Universitat de Barcelona, c/Martí i Franquès 1, 08028 Barcelona, Spain. E-mail: francesc.vines@ub.edu*

[b]*Institute of Functional Material Chemistry, Key Laboratory of Polyoxometalate Science of Ministry of Education, Faculty of Chemistry, Northeast Normal University, Changchun 130024, P. R. China. E-mail: yanlk924@nenu.edu.cn*

† Electronic supplementary information (ESI) available. See DOI: https://doi.org/10.1039/d3ta00261f

of the A element from a MAX phase precursor material, using F-containing etchants such as hydrofluoric acid (HF), or with HF produced *in situ* by mixing lithium fluoride (LiF) with hydrochloric acid (HCl). As a result, the as-synthesized MXenes display diverse surface functional groups on their basal planes, usually denoted as T_x, normally being –O, –OH, –H, or –F.[20,21] Aside from the above methods, F-free synthesis procedures have been reported,[22] with recent advances in controlling the surface termination with a variety of functionalities,[23] and even procedures and treatments to obtain MXenes with no surface termination.[23,24]

Note that these procedures may lead to the appearance of internal or external defects,[25] which, actually, can also be inherited from the precursor MAX phase. The presence of such defects can be affected by the synthesis methodologies and other factors, *e.g.* acid concentration, etching time, *etc.*,[26] and their existence may be influenced by the surface termination; *e.g.*, metal vacancy formation has been found to be more difficult on –O terminations than on –OH ones.[27] Still, given, normally, a low concentration of defects, the surface chemical activity of MXenes is mostly determined by regular, defect-free sites, and the surface terminations they display. Such MXenes have attracted considerable attention in heterogeneous catalysis given their high surface area, high electronic conductivity, and high chemical and catalytic activities, with abundant active sites, while their composition, width, and surface terminations are the sandbox based on which tailor-made MXenes can be set up for specific applications.[28]

In the particular context of the HER, previous theoretical and experimental studies have shown that some members of the MXene family are promising candidates for the HER.[18,29–34] However, these earlier computational studies assumed that the MXene basal plane functional group T_x consisted exclusively of either only –O or only –OH moieties, even though experimentally a diversity of –O, –OH, and –F moieties is detected.[35] Also, theoretical assessments point to mixtures of moieties as being energetically more stable.[36] In addition, MXenes have affinity towards H adatoms,[37] and water is an easy supplier of –H terminations,[38] even if it is difficult to unequivocally experimentally detect them. Actually, it is critical to realistically represent the MXene surface termination under HER working conditions of pH and applied potential, *U*. This aspect is crucial to understand the influence of the different types of functionalization in the HER potential determining step and the reaction mechanism. Here we focus on acidic environments, where proton (H^+) activity is larger, avoiding alkaline conditions where HER performance is found to be more sluggish.[39,40]

This is indeed tackled here on the prototypical Ti_3C_2 MXene, extensively experimentally synthesized with various functionalizations,[41–43] considering first the computed stability of hundreds of topologically different surface models with different ratios of –O, –OH, –H, and –F groups, used to build Pourbaix diagrams of surface termination stability dependent on pH and the applied potential, *U*. The obtained surface models suitable for HER conditions, considering both F-containing and F-free situations, allowed for a proper and detailed description of the reaction mechanism, highlighting (i) the presence of fluorine on the Ti_3C_2 surface unless obtained in F-absent situations, (ii) that, at variance with previous studies,[18,44–46] not only –O termination is regarded as a possible HER active site, but it may involve surface –OH groups, implying two different hydrogen sources, either protons (H^+) present in the medium, or surface H atoms, which make the reaction mechanism more complex, (iii) that –F groups can be beneficial at modulating the H bond strength, and not *per se* detrimental, and, finally, (iv) that the HER performance of the realistic models reveal that O-rich/OH-poor models, and stable ternary mixtures containing –F, –O, and –OH groups may lead to almost negligible estimated overpotentials, making such Ti_3C_2 terminated models excellent materials for the HER electrocatalysis.

2. Theoretical aspects

2.1. Computational details

The results reported in the present work were obtained from periodic density functional theory (DFT) calculations carried out using the Vienna *ab initio* simulation package (VASP).[47] The core electrons and their effect on the valence electron density were described by the projector augmented wave (PAW) method.[48] The exchange–correlation interaction was approximated by the Perdew–Burke–Ernzerhof (PBE) generalized gradient approximation functional.[49] A basis set of plane waves was used, employing a kinetic energy cutoff of 415 eV. An energetic electronic optimization convergence criterion of 10^{-5} eV was used, while atomic optimizations were finalized once all forces acting on atoms were below 0.01 eV $Å^{-1}$. The necessary numerical integrations in the reciprocal space were carried out using *k*-points *Γ*-centred Monkhorst–Pack meshes of $5 \times 5 \times 1$ dimensions.[50] The effect of dispersion was accounted for using Grimme's D3 approach (PBE-D3).[51] Note that present and past test calculations varying the optimization thresholds, *k*-point density, and the size of the basis set led to variations in the total energy well below chemical accuracy, *i.e.*, below ~0.04 eV —1 kcal mol^{-1}.[52] Vibrational frequencies of H_2 molecule in vacuum (see below) and the corresponding ones in the terminated Ti_3C_2 models were obtained by construction and diagonalization of the Hessian matrix, whose elements were computed by finite differences of analytical gradients with finite displacements of 0.03 Å in length. Note that such frequencies were obtained only for the terminations and adsorbed species, while atoms in the Ti_3C_2 MXene substrate were kept fixed in the optimized geometry. In this way, vibrational degrees of freedom on the surface terminations and adsorbed moieties are decoupled from Ti_3C_2 phonons, an approximation with negligible impact in the computed frequencies.[37,38,52]

Pristine and fully –O, –OH, –H, and –F covered Ti_3C_2 were firstly evaluated using a $p(2 \times 2)$ supercell. The cases mixing different moieties were evaluated using either a $p(2\times2)$ or a $p(3 \times 3)$ supercell. A maximum monolayer (ML) coverage is defined when having one surface moiety per each surface metal atom, four or nine for the $p(2 \times 2)$ or a $p(3 \times 3)$ supercell, respectively. In the case of the $p(2 \times 2)$ supercell, $\frac{1}{2}$ ML *vs.* $\frac{1}{2}$ ML binary coverages were evaluated, as well as $\frac{1}{4}$ *vs.* $\frac{3}{4}$ of a ML. Ternary situations were explored as well, considering $\frac{1}{4}$, $\frac{1}{4}$, and $\frac{1}{2}$ of a ML. For the $p(3 \times 3)$ supercell $\frac{1}{3}$ *vs.* $\frac{2}{3}$ binary situations were

examined, as well as ternary situations with $\frac{1}{3}$ of each component. The slab models contained 20 Å of vacuum to properly isolate the models explored.

2.2. HER reaction mechanisms

In general, there are two possible well-agreed mechanisms for the HER reaction, namely the Volmer–Tafel and Volmer–Heyrovsky mechanisms.[53] In both cases, the first step is the same, the Volmer step, where a proton, H^+, is reduced on the electrocatalytic surface by an electron, e^-;

$$H^+ + e^- + * \rightarrow H^*, \quad (1)$$

where * represents a surface electrocatalytic active site. However, the two mechanisms differ in the second step: in the Volmer–Tafel mechanism, the Tafel step implies that two previous Volmer steps have occurred, and, so, two reduced H* entities exist. These can then combine in a chemical step —with no further electron transfer—to create a H_2 molecule which is directly desorbed from the electrocatalyst surface;

$$2H^* \rightarrow H_2 + 2^*. \quad (2)$$

Notice that this mechanism is somehow similar to the Langmuir–Hinshelwood one in gas-phase heterogeneous catalysis, *i.e.*, all reactants must first adsorb, prior to the reaction among them. Furthermore, one should be aware that generally the Volmer–Tafel mechanism does not consider the H_2* moiety, *i.e.*, it assumes that whenever H_2 is formed, it automatically desorbs. Still, in case the H_2 molecule is moderately adsorbed, one could rephrase the full Volmer–Tafel mechanism as

$$(2\times)\ H^+ + e^- + * \rightarrow H^*, \quad (3)$$

$$2H^* \rightarrow H_2^* + *, \quad (4)$$

$$H_2^* \rightarrow H_2 + *. \quad (5)$$

In the Volmer–Heyrovsky mechanism, the second proton is reduced directly over the previously reduced proton of the previous Volmer step, directly generating, again, the H_2 molecule. Thus

$$H^* + H^+ + e^- \rightarrow H_2 + *. \quad (6)$$

Indeed, this mechanism is reminiscent of the Eley–Rideal mechanism in gas-phase heterogeneous catalysis; *i.e.*, only one reactant is adsorbed, and the other one directly attacks the adsorbed one from the gas phase. Still, the H_2* moiety is generally ignored, but the Volmer–Heyrovsky mechanism could be rewritten as

$$H^+ + e^- + * \rightarrow H^*, \quad (7)$$

$$H^+ + e^- + H^* \rightarrow H_2^*, \quad (8)$$

$$H_2^* \rightarrow H_2 + *. \quad (9)$$

In the present study we regarded all the possible reaction mechanisms and elementary reaction steps, although in most examples in the literature,[18,44–46] the Volmer–Heyrovsky was the only mechanism considered, and, moreover, regarding only the H reduction on fully O-terminated MXenes, like $Ti_3C_2O_2$, even when high H coverage situations were involved. Thus, in addition to O-termination, we regarded –H, –OH, and –F full terminations, and binary and ternary combinations of them, as explained above. Notice that the inclusion of –OH and –H terminations implies that the reaction sequence can involve hydrogen atoms from surface terminations. Thus, instead of starting through the reduction of one or two H^+ from the aqueous medium, for either Volmer–Heyrovsky or Volmer–Tafel mechanisms, the reaction may start through one or two H atoms of –OH and/or –H terminations. For example, on a –OH terminated Ti_3C_2, the Volmer–Heyrovsky reaction sequence could well be

$$H^+ + e^- + –OH \rightarrow –O + H_2^*, \quad (10)$$

$$H_2^* \rightarrow H_2 + *, \quad (11)$$

$$H^+ + e^- + –O \rightarrow –OH. \quad (12)$$

Notice that the direct formation of water upon a Volmer step on a surface –OH moiety has been disregarded as competitive since water removal requires the energetic cost of a surface O removal, plus free MXene surface sites are known to very easily adsorb H_2O and dissociate it.[38,54] While for the Volmer–Tafel mechanism, the formation of H_2 from two H atoms from –OH surface groups could occur first, and then followed by the regeneration of the –OH moieties. Thus

$$2–OH \rightarrow 2–O + H_2^*, \quad (13)$$

$$H_2^* \rightarrow H_2 + *, \quad (14)$$

$$(2\times)\ H^+ + e^- + –O \rightarrow –OH. \quad (15)$$

In the present work, all these alternative reaction step sequences have been thoroughly investigated in all the surface models, to have a clear, holistic picture of the reaction mechanism.

2.3. Thermodynamic approach

For any of the above-mentioned mechanisms, we first consider the reaction thermodynamic profile by calculating the Gibbs free energy of hydrogen adsorption, obviously considering only minima in the potential energy surface. Note that the deliberate use of this approach neglects further kinetic aspects, succinctly assuming that energy barriers are simply differences in Gibbs free energies between minima. This approach has to be taken with a grain of salt, since, on one hand, one neglects that electrochemical steps involve a transition state, and the involved energy barriers will be larger than Gibbs free energy differences. The thermodynamic approach can be justified from the Brønsted–Evans–Polanyi (BEP) relationship that usually holds true,[55,56] and so energy barriers would be linearly

proportional to the Gibbs free energy difference, although bearing in mind the kinetics on the coupled proton–electron transfer steps may imply breaking these relationships. In any case, the kinetic aspects could be important, as shown, *e.g.*, in the chlorine evolution reaction (CER), oxygen evolution reaction (OER), and oxygen reduction reaction (ORR).[57,58] Further than that, other aspects could be critical in the proper HER performance, such as mass transport limitations.[7] In any case, such detailed analyses are out of the scope of the present study, which aims at determining how surface terminations affect the HER reaction landscape, and for that we rely on the thermodynamic approach as a first educated guess, as extendedly used in the past.[5,6,11–13,18,24–29]

Following the seminal work of Nørskov *et al.* introducing the computational hydrogen electrode (CHE),[59] one can consider standard equilibrium conditions of pH = 0, $U = 0$ V, temperature, T, of 298.15 K, and a partial pressure of H_2, p_{H_2}, of 1 bar. Under these standard working conditions, the complete HER pathway can be described as

$$H_{(aq)}{}^{+} + e^{-} \rightarrow \tfrac{1}{2}H_2^{(g)},\ \Delta G^{\circ} = 0\ \text{eV}, \tag{16}$$

where the chemical potentials or Gibbs free energies of the initial state, that is $H^{+}_{(aq)} + e^{-}$, and that of the product, $\frac{1}{2}H_2^{(g)}$, are identical. Also, for any reaction intermediate, one can get the ΔG, *e.g.*, for adsorbed H*, one obtains ΔG_H as

$$\Delta G_H = \Delta E_H + \Delta E_{ZPE} - T\Delta S_{H,} \tag{17}$$

where ΔE_H is the reaction step energy difference, ΔE_{ZPE} the change in zero point energy (ZPE), and ΔS_H the change in entropy upon adsorption. The ΔE_H term can be easily obtained from the total energies obtained during the computational optimizations, so that

$$\Delta E_H = E_{nH/MXene} - E_{(n-1)H/MXene} - \tfrac{1}{2}E_{H_2}, \tag{18}$$

where $E_{nH/MXene}$ is the total energy of n H adatoms adsorbed on the MXene model, $E_{(n-1)H/MXene}$ the corresponding energy on a model having $n - 1$ H adatoms, and E_{H_2} the energy of a H_2 molecule in vacuum. Likewise, the ΔE_{ZPE} term is obtained as

$$\Delta E_{ZPE} = E^{ZPE}_{nH/MXene} - E^{ZPE}_{(n-1)H/MXene} - 1/2E^{ZPE}_{H_2}, \tag{19}$$

where $E^{ZPE}_{nH/MXene}$, $E^{ZPE}_{(n-1)H/MXene}$, and $E^{ZPE}_{H_2}$ are the ZPE energies of the MXene having n adsorbed H adatoms, $n - 1$ adsorbed H adatoms, or the H_2 molecule in vacuum, respectively. The ZPE energy term, E^{ZPE}, is obtained from the computed vibrational frequencies, so that

$$E_{ZPE} = \frac{1}{2}\sum_{i=1}^{NMV} h\nu_i, \tag{20}$$

where h is the Planck's constant, and ν_i the vibrational frequency of each of the normal modes of vibration (NMVs), taken, for a system having N atoms, as $3N - 5$ for the linear H_2 molecule in vacuum, and $3N$ for adsorbed atoms/molecules, since free translations and rotations become frustrated vibrational modes upon adsorption. Similar to ΔE_H, the ΔS_H term is calculated as

$$\Delta S_H = S_{nH/MXene} - S_{(n-1)H/MXene} - \tfrac{1}{2}S_{H_2}, \tag{21}$$

where $S_{nH/MXene}$, $S_{(n-1)H/MXene}$, and S_{H_2} are the entropies of the MXene model having n H adatoms, the MXene model having $n - 1$ H adatoms, and the H_2 molecule in vacuum, respectively. The gas phase entropy of H_2, 130.68 J mol^{-1} K^{-1} has been taken as tabulated in the National Institute of Standards and Technology (NIST) webbook,[60] while for the adsorbed moieties only the vibrational entropy, S_{vib}, is accounted for, given the ground state character and the aforementioned frustration of translations and rotations upon adsorption.[61] Thus

$$S = S_{vib} = k_B\sum_{i=1}^{NMV}\ln\left(1 - e^{-\frac{h\nu_i}{k_BT}}\right) - \sum_{i=1}^{NMV} h\nu_i\left(\frac{1}{e^{\frac{h\nu_i}{k_BT}} - 1}\right), \tag{22}$$

where k_B is the Boltzmann's constant.

2.4. Surface Pourbaix diagrams

The Pourbaix diagram analysis is a key aspect to be regarded since the diagrams provide information about the surface composition under electrocatalytic conditions. In the case of the studied MXenes they allow determining which is the thermodynamically most stable surface termination under working conditions of pH and U.[62] Details of the computational estimate of these diagrams can be found elsewhere,[63] but let us here briefly explain the procedure. For any surface composition, the ΔG of formation is obtained, using certain molecular references. In the present case, one uses $H_2^{(g)}$ and $F_2^{(g)}$ references at 1 bar and 298.15 K for –H and –F terminations, using the standard hydrogen electrode (SHE) and standard fluorine electrode (SFE) under equilibrium conditions, so that

$$H^{+}_{(aq)} + e^{-} \leftrightarrow \tfrac{1}{2}H_2^{(g)}, \tag{23}$$

$$\tfrac{1}{2}F_2^{(g)} + e^{-} \leftrightarrow F^{-}_{(aq)}. \tag{24}$$

Here, values of 0 and −2.87 eV are used for the reduction potentials of hydrogen, U, and of fluorine, U_F, respectively.[64] In the case of –OH and –O terminations, water vapor is used as a reference, taken at 0.035 bar and 298.15 K, conditions under which water vapor is in equilibrium with liquid water, that is, their chemical potentials or Gibbs free energies are equal.[59] The computational Pourbaix diagram construction makes use of the CHE[63] and the computational fluorine electrode (CFE), so that, under the aforementioned equilibrium conditions

$$\mu\left(H^{+}_{(aq)}\right) + \mu(e^{-}) = G\left(H^{+}_{(aq)}\right) + G(e^{-}) = \frac{1}{2}G\left(H_2^{(g)}\right), \tag{25}$$

$$\mu\left(F^{-}_{(aq)}\right) - \mu(e^{-}) = G\left(F^{-}_{(aq)}\right) - G(e^{-}) = 1/2G\left(F_2^{(g)}\right), \tag{26}$$

where μ and G are simply the chemical potentials or Gibbs free energies of the specified species.

Making use of these references and of the gas phase ones, one can calculate the formation energy of a given surface termination at zero pH and U, $\Delta G(0,0)$, as

$$\Delta G(0,0) = \Delta G = \Delta E + \Delta E_{ZPE} - T\Delta S, \quad (27)$$

with the different contributions obtained in a similar fashion as detailed above for ΔG_H, and gas phase molecule entropy taken from thermodynamic tables.[65] Once $\Delta G(0,0)$ is obtained, the pH and U dependent ΔG, $\Delta G(\mathrm{pH},U)$, can be obtained, as derived,[63,66] from the following equation:

$$\Delta G(\mathrm{pH},U) = \Delta G(0,0) - \upsilon(\mathrm{H^+})k_B T \ln 10\ \mathrm{pH} - \upsilon(\mathrm{e^-})eU - \upsilon(\mathrm{F^-})eU_F, \quad (28)$$

where $\upsilon(\mathrm{H^+})$, $\upsilon(\mathrm{F^-})$, and $\upsilon(\mathrm{e^-})$ are the stoichiometric coefficients of the formation chemical equation. As an example, let us take a $p(3 \times 3)$ slab with 9 free surface sites, *. Thus, the formation of a surface having 3 O* and 6 F* would read as

$$3H_2O + 3F_2 + 9^* \rightarrow 3O^* + 6F^* + 3H_2, \quad (29)$$

for the $\Delta G(0,0)$ term considering gas phase species, but when considering pH and U, and the presence of H^+ and F^- species in solution, the equation can be rewritten as

$$3H_2O + 6F^- + 9^* \rightarrow 3O^* + 6F^* + 6H^+ + 12e^-, \quad (30)$$

where $\upsilon(\mathrm{H^+})$, $\upsilon(\mathrm{F^-})$, and $\upsilon(\mathrm{e^-})$ would be 6, –6, and 12, respectively.

Following the above recipe, one can get the ΔG for any surface termination as a function of pH and U. Thus, the relative stability of different terminations under realistic conditions can be determined, the most stable at a given pH and U being the one with the lowest ΔG. Such info can be used to draw the Pourbaix diagrams by either making a fine grid of points and evaluating ΔG values of all the explored situations while taking the minima, or finding equilibrium lines in between competing surface terminations, for conditions in between phases A and B where $\Delta G(\mathrm{A}) = \Delta G(\mathrm{B})$. Note that, computationally, one can directly relate the computed ΔG_s when using the same supercell; however, it is worth pointing out that, when using different supercells, ΔG_s must be normalized and compared as given per surface area.

3. Results and discussion

3.1. Surface termination analysis

Prior to finding suitable models for evaluating the HER on Ti_3C_2 MXene, the four different surface termination moieties, namely –O, –OH, –H, and –F were considered on the Ti_3C_2 $p(3 \times 3)$ supercell at high-symmetry top metal (T), bridge (B), three-fold hollow C (H_C), and three-fold hollow Ti (H_{Ti}) positions, see Fig. 1, thus sampling at low-coverage regimes. Along with previous records with the same computational setup,[37,38,52] the H_{Ti} site is regularly preferred. To further confirm the preference of surface termination moieties towards H_{Ti} sites, the full –OH terminated and a mixture of $\frac{2}{3}$ of –O and $\frac{1}{3}$ of –OH were examined here, both occupying H_C or H_{Ti}, finding a clear preference for the latter by −0.23 to −0.64 eV per moiety unit, respectively, see Fig. S1 in the ESI.† Accordingly, the posterior surface termination samplings were examined only on H_{Ti} sites.

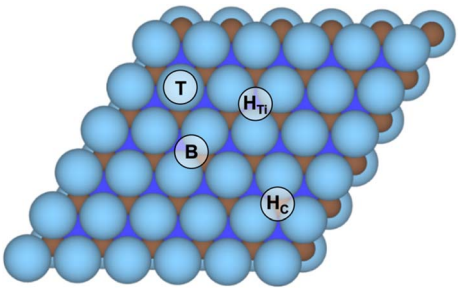

Fig. 1 Top view of the Ti_3C_2 MXene model (0001) surface, where brown spheres denote C atoms, and light and dark blue spheres surface and subsurface Ti atoms, respectively. High-symmetry sites are tagged.

In this way, 95 different surface terminations were explored considering mono, binary, and ternary situations combining –OH, –O, –H, –F, and free sites. For binary and ternary cases, different surface compositions were also considered, and for each one, different topologically distinct arrangements were studied, see Fig. S2–S7 in the ESI,† leading to a final number of 385 distinct surface terminations, making the present study the most complete so far regarding Pourbaix diagram evaluation of the Ti_3C_2 MXene model (0001) surface.[63]

Let us start the discussion with the simplest Pourbaix diagrams, regarding only full coverage situations of –O, –OH, –H, or –F. Fig. 2 shows two versions either considering F-free synthesis, thus in the absence of fluorine anions,[67–69] or regarding fluorine explicitly useful, *e.g.*, for MXenes synthesized using HF or *in situ* HF.[19–21] The Pourbaix diagrams in Fig. 2 agree with previous assessments,[18,70] particularly in the sense that generally the Ti_3C_2 (0001) surface is O-terminated at positive U with respect to the reversible hydrogen electrode (RHE) reference, or, in other words, above the HER equilibrium potential line, noting that, just below it, the –OH termination is preferred, in accordance with a favorable H^+ reduction. Only at very negative potentials the H-termination becomes preferable, while free surface metal sites without termination are never found to be preferred. The equilibrium line in between –O and –OH terminations is actually very close to the HER equilibrium line, which suggests the existence of binary systems in between. Finally, note that –F has a small, yet key region of influence around the HER equilibrium line, particularly for very low pH values, up to pH = 2, exactly the region where HER conditions are sought, *i.e.*, U values close to the HER equilibrium line, and a strong acidic medium, with a high concentration of H^+ reactant. Thus, binary and even ternary surface terminations are in principle to be considered in duly modeling the HER on the Ti_3C_2 (0001) surface, and at this stage only free sites and –H terminations could be, in principle, ruled out, unless working at very low U.

In order to explicitly address this issue, the aforementioned mixed terminations were considered, and the resulting

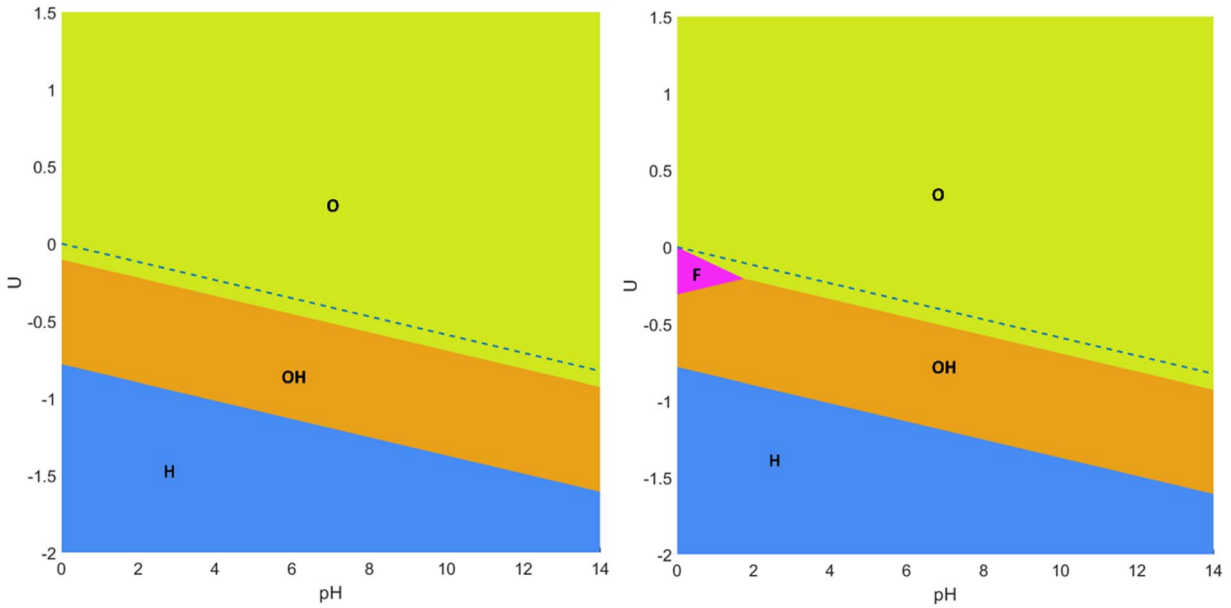

Fig. 2 Pourbaix diagrams for the Ti_3C_2 MXene (0001) surface regarding fully –O, –OH, and –H terminated surfaces (left), or including as well fully –F terminated surfaces (right). Regions of preferred stability are colored and tagged. The blue, dashed line indicates the HER equilibrium potential using the RHE.

Pourbaix diagrams, either for F-containing or F-free situations, are shown in Fig. 3. From these diagrams, several aspects need to be pointed out. On one hand, the large regions of fully –O, –OH, or –H terminations as observed in the simplified Pourbaix diagrams of Fig. 2 are not realistic, and mixed situations constitute actually the preferred situation in the vicinity of the HER equilibrium line. Thus, the O-termination just above the HER equilibrium line, commented when discussing Fig. 2, is indeed an O-rich case, but containing a fraction of OH moieties, as observed by the sequential preference of the $O_{2/3}OH_{1/3}$ model, followed by the $O_{3/4}OH_{1/4}$ model, and only fully –O terminations are found *ca.* 0.4 V above the HER equilibrium line. Likewise, the –OH region under the HER equilibrium line in Fig. 2 is, in fact, an OH-rich mixture as denoted firstly by the

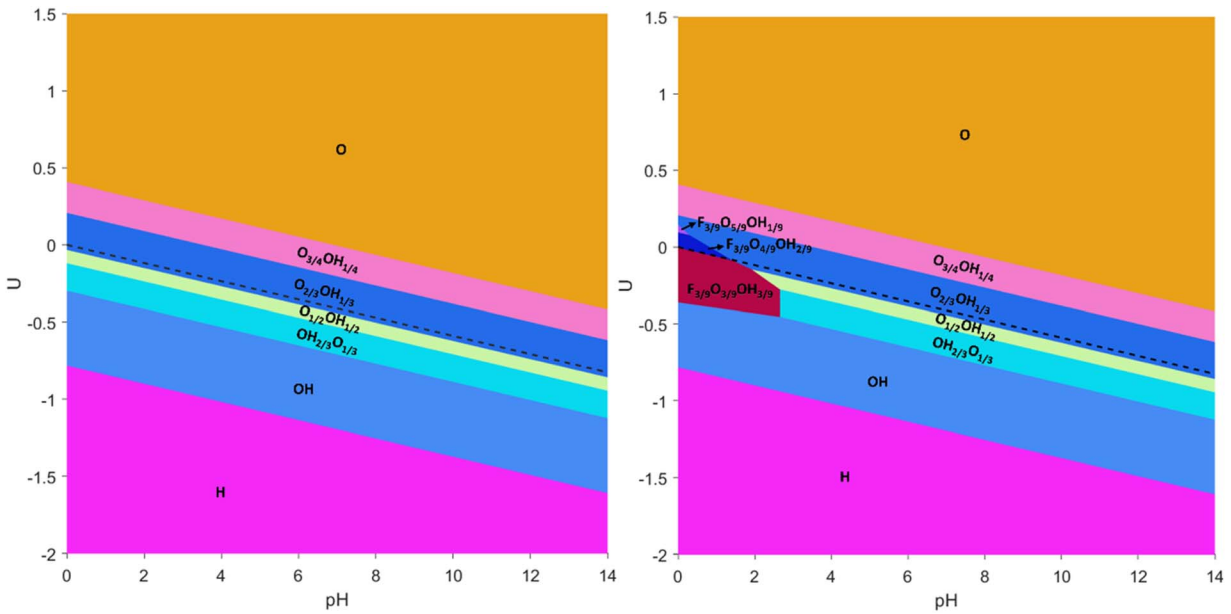

Fig. 3 Pourbaix diagrams for the Ti_3C_2 MXene (0001) surface regarding all single, binary, and ternary surface compositions including –O, –OH, –H, and –F terminations, as well as free sites. The left image corresponds to situations without any –F termination, while the right image corresponds to situations when considering –F termination. The black, dashed line indicates the HER equilibrium potential with respect to the RHE reference.

$OH_{1/2}O_{1/2}$ model, followed by the $OH_{2/3}O_{1/3}$ model, and only the fully –OH model is found *ca.* −0.3 V below the HER equilibrium line. Only by going to more negative potentials, more than −0.8 V below the HER equilibrium line, would one reach the fully –H terminated model.

Moreover, the present F-free Pourbaix diagram, see Fig. 3, reinforces previous assessments[18,63] in which in the vicinity of HER equilibrium conditions the Ti_3C_2 (0001) surface involves a mixture of –O and –OH terminations, –OH rich at *U* values more negative than HER equilibrium line and –O rich at U values more positive than HER equilibrium line, but essentially ruling out having fully –O terminated Ti_3C_2 as a viable model for the HER.[71,72] Furthermore, the –OH termination is just preferred over a certain potential margin, and not stable at very low potentials as sometimes claimed in the literature,[18] neither essentially non-existing as pointed out in others,[63] plus the fully –H termination is viable at very low potentials, rather than the ideal, non-terminated surface.[18]

Still, the obtained Pourbaix diagram underscores the O-affinity of the Ti_3C_2 (0001) surface, plus the H-affinity of $Ti_3C_2O_2$, given the appearance of a certain ratio of –OH moieties above the HER equilibrium line. As forecasted from fully single-terminated situations in Fig. 2, the Pourbaix diagram becomes disrupted when regarding –F moieties, see Fig. 3. There, one has to first highlight the stability of the $F_{1/3}O_{1/3}OH_{1/3}$ model up to a pH of 2.87 and particularly close but below the HER equilibrium line, shown as a black dashed line in Fig. 3, with the region of prevalence of $F_{1/3}O_{1/3}OH_{1/3}$ being exactly the ideal conditions to carry out the HER. Actually, a previous study[73] claimed that the HER catalytic activity of Ti-based MXenes is experimentally and computationally correlated with the ratio of –F and –O functional groups, where large amounts of –F show poor catalytic activity and selectivity compared to low amounts of –F, plus the observation that a monotonous increase of –O termination increases the electrochemical potential.

In any case, the above commented Pourbaix diagram already underscores the need to account for such –F moieties, at least on $Ti_3C_2T_x$, when obtained through F-containing synthetic procedures. To further inspect this, additional ternary models containing –F, –O, and –OH moieties were calculated by increasing or decreasing the –O/–OH ratio, that is, through $F_{3/9}O_{5/9}OH_{1/9}$, $F_{3/9}O_{4/9}OH_{2/9}$, $F_{3/9}O_{2/9}OH_{4/9}$, and $F_{3/9}O_{1/9}OH_{5/9}$ models. These four models involved the systematic exploration of the topologically different arrangements, see Fig. S8 and S9 in the ESI,† accounting for 64 extra surface terminations. The impact of these terminations is only observed at very low pH and just above the HER equilibrium line, where small regions are observed for the $F_{3/9}O_{4/9}OH_{2/9}$ and $F_{3/9}O_{5/9}OH_{1/9}$ models, in which the presence of –F is maintained, while the surface becomes –O richer at the expense of the –OH groups. In any case, Fig. 3 reveals a number of surface terminations that could be relevant in the HER, either for F-containing or F-free $Ti_3C_2T_x$.

One still has to keep in mind that the present Pourbaix diagrams are the result of a series of terminations and topological arrangements that are anyway constrained by the employed supercells, and so, other arrangements could and would be possible. Besides, situations shown in Fig. 3 correspond to the most stable cases, but there are other arrangements which are close in energy that could well be appearing on the surface, especially when having in mind the inherent energy accuracy limitation of DFT-based calculations. Thus, a number of close possibilities should be regarded when inspecting the HER on $Ti_3C_2T_x$, as shown in detail below.

Last but not least, when considering the terminations in Fig. 2 and 3 for electrocatalytic HER applications, one should first regard whether the material remains conductive, or becomes a semiconductor, since the latter would handicap the electronic transference. To tackle this issue, the density of states (DOS) and projected DOS (PDOS) were obtained and are shown in Fig. S10 of the ESI,† revealing, briefly, that pristine Ti_3C_2, any fully terminated $Ti_3C_2T_x$, and any binary or ternary combinations of surface terminations lead to a metallic system, with the characteristic bonding, non-bonding, and anti-bonding regions of parent three-dimensional transition metal carbide (TMC) bulk structures,[74] with the participation of Ti d orbitals, C and T_x = O, OH, F p orbitals, and H s orbitals. Notice that by mixing Ti d states with O, OH, F p or H s orbitals, new states appear close to the Fermi level, E_F, arising from terminations, which may have a key impact in the H^+ adsorption, and, consequently, on the HER electrocatalysis.

Aside from the above, charge density difference (CDD) plots, shown in Fig. S11 of the ESI,† reveal that, while Ti atoms become positively charged at the expense of giving their electron density to C atoms,[75] any –O, –OH, –H and –F groups also become negatively charged, again at the expense of the electron density of surface Ti atoms. This leads to charge accumulations which are more prominent for –O terminations, compared to –F and –OH groups, in line with a formal $-2e$ charge of O adatoms, while –F and –OH would have a charge close to $-1e$. In the case of –H, there is some electron accumulation, but more attenuated. Finally, on the binary and ternary systems, one clearly observes charge distributions, which can be easily interpreted as compatible with local rearrangements similar to the just mentioned full-terminated cases.

3.2. HER electrocatalysis mechanisms

Having established the surface stabilities through the computationally derived Pourbaix diagrams, and the overall electronic picture, it is now the turn of inspecting the HER performance on selected, representative cases. Let us begin with pristine Ti_3C_2 and fully terminated cases, that is, with –O, –OH, –F, and –H terminations. As aforementioned, both Volmer–Heyrovsky and Volmer–Tafel mechanisms are studied, and also considering the possible involvement of H atoms from –H and –OH terminations. Fig. 4 shows the Gibbs free energy reaction profiles for these five cases under standard working conditions —T = 298.15 K, p_{H_2} = 1 bar, pH = 0, U = 0 V— regarding different reaction mechanisms and sequences, depending on whether surface termination coming from –H or –OH groups is involved or not.

Let us first inspect the most extreme surface termination, which would be pristine Ti_3C_2. Pristine Ti_3C_2 is excessively chemically active, binding too strongly to the H adatom, with

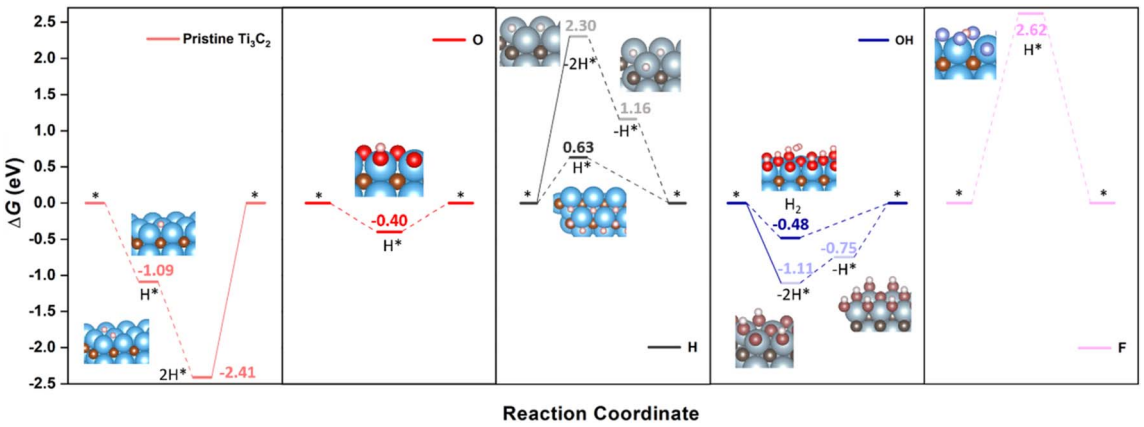

Fig. 4 Gibbs free energy, ΔG, diagram of the HER on pristine or fully –O, –OH, –F, or –H terminated Ti_3C_2 (0001) surface under standard working conditions. Solid lines represent the chemical step of the as-generated H_2 desorption, while dashed lines represent the electrochemical steps of proton coupled electron transfer (PCET). Inset images are side or eagle-eye views of the reaction intermediates, except for the H* state on –H termination, which depicts a top view to better observe the H* allocation on a surface empty H_C site. Color coding as in Fig. 1, plus H, O, and F atoms are shown as white, red, and violet spheres. Preferred reaction mechanism and associated images are shown with bright coloring, while shadowed colors and images refer to other, non-preferred mechanisms.

sequential computed ΔG_s of −1.09 and −1.32 eV for the reduction of two protons following a Volmer–Tafel mechanism. Even though the two proton coupled electron transfers (PCETs) are energetically downhill, the formation of $H_2^{(g)}$ through the H* recombination in a chemical step is uphill by 2.41 eV, which implies a prohibitive annealing while trying to maintain the electrochemical conditions. Here basically the pristine Ti_3C_2 (0001) surface would be too reactive, and would successively reduce protons or hydroxyl groups coming from water so as to achieve a suitable surface termination according to the Pourbaix diagram (*cf.* Fig. 3). On the other extreme, one would have the –F terminated Ti_3C_2 surface with a severely decimated H-affinity, and a greatly unfavored first H^+ reduction, with a ΔG = 2.62 eV, which could only work by applying a negative U of −2.62 V to lower the first electron transfer. The second PCET would rather follow here the Volmer–Heyrovsky mechanism. This result goes along with the aforementioned statement that large amounts of –F surface moieties imply poorer electrocatalytic activities and selectivities.[73]

Focusing on more suited surface terminations, the –O termination chemical activity gets attenuated in a large proportion, featuring a ΔG of −0.40 eV for first H^+ reduction following the Volmer–Heyrovsky mechanism, thus requiring a U of −0.40 V to reduce the energetic costs of the second PCET, although at such overpotentials, the Ti_3C_2 surface would be mostly terminated by –OH groups, see Fig. 2 and 3. Actually, when inspecting –OH termination, the reaction energetics and mechanism already become more complicated. On one hand, one could consider a situation where two neighboring –OH termination moieties react to create two –O moieties plus a $H_2^{(g)}$ molecule. This chemical step has a ΔG of −1.11 eV, and would be followed by two consecutive H^+ reductions on the as-generated –O termination sites to regenerate the electrocatalyst surface. In the literature, the corresponding overpotential is calculated, whenever considered, assuming that both H^+ reduction steps are equally costly, and so the applied overpotential would be *ca.* −0.56 V, while the direct H^+ reduction on an –OH surface moiety, following a Volmer–Heyrovsky mechanism, to directly generate $H_2^{(g)}$ has a ΔG of −0.48 eV, to be followed by the reduction of a H^+ on the as-generated –O moiety to regenerate the electrocatalyst surface.

By this simpler view, one would consider that both mechanisms, considering one or two –OH terminations, could be somewhat competitive, differing by only 0.08 eV in the potential determining step, with a preference though on the Volmer–Heyrovsky mechanism. However, a closer inspection of the mechanism involving two surface –OH terminations leads to an easier first H^+ reduction, with a ΔG of 0.36 eV, while the second H^+ reduction is more costly, with a ΔG of 0.75 eV, acting as a rate and potential determining step. Thus, a Volmer–Heyrovsky reaction sequence as depicted in eqn (10)–(12) seems to be the most preferred one in –OH terminated Ti_3C_2, with a U of 0.48 V, in line with the overpotential of the OH-terminated phase as seen in the Pourbaix diagrams of Fig. 3.

Finally, in the H-terminated model, the Volmer–Tafel mechanism involving first the –H moiety recombination is found to be energetically quite costly, by 2.30 eV, making it prohibitive, even though the posterior electrocatalyst regeneration is quite downhill, with first and second H^+ reduction steps involving ΔG_s of −1.14 and −1.16 eV, respectively. Actually, on a fully H-terminated Ti_3C_2 (0001) model, the first H^+ reduction is a Volmer step, occupying a H_C site, with no direct formation of $H_2^{(g)}$, and with a ΔG of 0.63 eV, while the second H^+ reduction would follow a Heyrovsky step. Note here as well that the potential determining step implies a U of −0.63 V, which is close to the region of prevalence of –H termination on the Pourbaix diagrams, see Fig. 3.

However, as seen in Fig. 3, at low pH and seeking low U working values, one should not use the fully terminated models, and consider models with binary and/or ternary situations, depending on whether one would have fluorine or not. This is evaluated in Fig. 5 for a list of suitable terminations derived

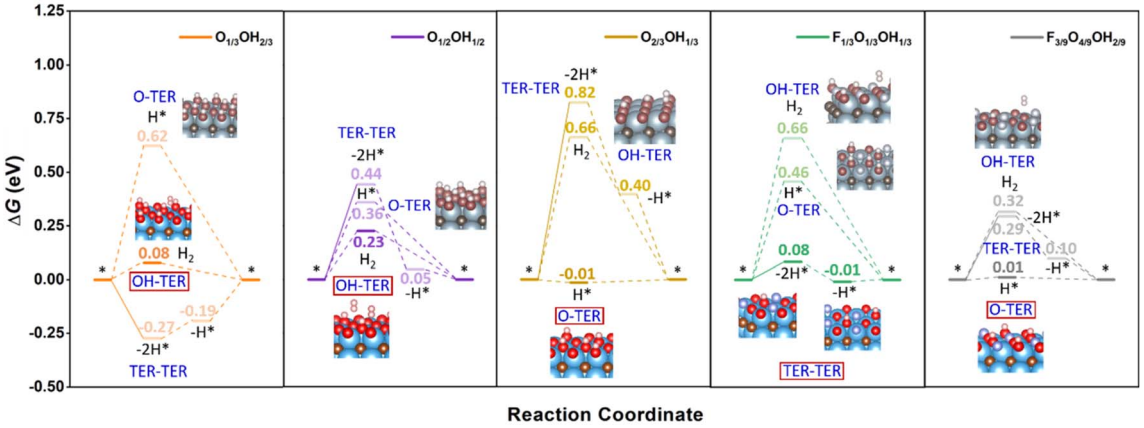

Fig. 5 Gibbs free energy, ΔG, diagram of the HER on selected binary and ternary terminations of the Ti_3C_2 (0001) surface combining –O, –OH, and –F moieties, under standard working conditions. Solid lines represent the chemical step of the as-generated H_2 desorption, while dashed lines represent the electrochemical PCET steps. Color coding as in Fig. 4.

from the realistic Pourbaix diagrams including F-free $O_{1/3}OH_{2/3}$, $O_{1/2}OH_{1/2}$, and $O_{2/3}OH_{1/3}$, but also the F-containing $F_{1/3}O_{1/3}OH_{1/3}$ and $F_{3/9}O_{4/9}OH_{2/9}$ models. Focusing on F-free models, one has different proportions of –O and –OH moieties, but their mutual existence opens three possible reaction mechanisms; (i) the H^+ reduction occurs on an –O site, followed by a Heyrovsky step on top to directly generate $H_2^{(g)}$, hereafter denoted as O-TER, (ii) the H^+ reduction occurs on a –OH site, following a Heyrovsky step, and a subsequent H^+ reduction on the as-generated free –O site, hereafter denoted as OH-TER, and (iii) a Tafel step between two surface –OH moieties, followed by two subsequent Volmer steps to regenerate the –OH sites, by reducing the as-freed –O sites, named TER–TER.

Keeping this in mind, the $O_{1/2}OH_{1/2}$ model shows a TER–TER profile where $H_2^{(g)}$ formation is moderately costly, by $\Delta G = 0.44$ eV, followed by two consecutive H^+ reductions with ΔG values of -0.39 and -0.05 eV, respectively. Actually, the first chemical step in this mechanism is unavoidably endergonic, and cannot be reduced by a potential application, which could otherwise lower the electrochemical steps just by applying a U of -0.05 V. This does not happen in either the OH- or the O-TER mechanism. In the latter, the first Volmer step has a positive ΔG of 0.36 eV, higher than that of the Heyrovsky step of OH-TER of ΔG 0.23 eV. Thus, the OH-TER path could make the full process exergonic by applying a U of -0.23 V, close to the $O_{1/2}OH_{1/2}$ stability region on the F-free Pourbaix diagram in Fig. 3.

The results discussed just above involve a model with equal number of –OH and –O groups; by unbalancing this ratio by having more –O groups, like in the $O_{2/3}OH_{1/3}$ model, see Fig. 5, the TER–TER mechanism gets more endergonic in the first Tafel step, with a ΔG of 0.82 eV, and even the first replenishment H^+ reduction Volmer step, with ΔG of -0.42 eV, is located 0.40 eV above the equilibrium $\Delta G = 0$ eV line, and so a U of -0.42 V would be needed to make the full process exergonic. The same situation is found in the OH-TER mechanism, where the first Heyrovsky step involves a ΔG up to 0.66 eV. Thus, compared to the $O_{1/2}OH_{1/2}$ model, the Tafel step increases in free energy by 0.38 eV and the OH-TER Heyrovsky step by a similar 0.43 eV. On the other hand, compared to the U of -0.23 V in the $O_{1/2}OH_{1/2}$ model, the O-TER step has a first Volmer step of solely -0.01 eV, implying the need of a U only slightly more negative than -0.01 V to make the full process exergonic. Clearly, the imbalance towards increasing the number of –O moieties favours the O-TER mechanism, while it is a handicap to the other mechanisms involving –OH moieties, namely, the OH-TER and TER–TER, plus the resulting overpotential falls well within the stability region of the $O_{2/3}OH_{1/3}$ model, quite in the HER equilibrium line, see Fig. 3.

Compared to the $O_{1/2}OH_{1/2}$ model, when the –O/–OH ratio imbalance is applied in the other direction, that is, when having more –OH moieties than –the O ones, as in the $O_{1/3}OH_{2/3}$ model, the O-TER is destabilized, with a first Volmer step rising up 0.26 eV up to a value of 0.62 eV. On the other hand, the OH-TER path gets its Heyrovsky step stabilized by 0.15 eV to a final value of $\Delta G = 0.08$ eV. Finally, the TER–TER path changes from being quite endergonic in the recombination chemical step of 0.44 eV in the $O_{1/2}OH_{1/2}$ model, to sensibly exergonic by -0.27 eV in the OH-rich $O_{1/3}OH_{2/3}$ model. In the last situation, the OH-TER path is preferred, with a potential determining step of $U = -0.08$ V, while on the TER–TER path, a U of -0.19 V for the second PCET is required to make the full process exergonic. Particularly, the overpotential of the last mechanism falls within the $O_{1/3}OH_{2/3}$ stability line as shown in the Pourbaix diagram of Fig. 3.

Up to this point, we tackled F-free models only, but the question regarding the effect of –F moieties on the HER performance remains open. Let us first address the $F_{1/3}O_{1/3}OH_{1/3}$ model which is the most stable one at low pH and low U with respect to the RHE (*cf.* Fig. 3). Here one can compare with the $O_{2/3}OH_{1/3}$ reference, where half of the –O moieties are replaced by –F groups. Consequently, the observed stabilization of the O-TER path under the O-rich conditions in the $O_{2/3}OH_{1/3}$ model is decimated and, consequently, the H* intermediate after a Volmer step involves a ΔG increase of 0.47 eV up to a final value of 0.46 eV. A similar effect is observed on the OH-TER and

TER–TER paths when compared to the OH-rich $O_{1/3}OH_{2/3}$ reference. The stabilization of such paths involving –OH groups is now hampered, making it rise the Heyrovsky step of OH-TER by 0.58 eV up to a final value of 0.66 eV. However, this is not so adverse for the TER–TER path, which was slightly exergonic. In the $F_{1/3}O_{1/3}OH_{1/3}$ model, the chemical H* recombination step is barely endergonic by 0.08 eV, and the potential determining step is the second recovering Volmer step requiring only a U of −0.01 V, ideally fitting in the model stability region shown by the Pourbaix diagram (*cf.* Fig. 3), and essentially matching the HER equilibrium potential *vs.* RHE. Here the –F surface moiety has no longer been considered as the active site given the very high overpotential found in the fully –F terminated model of 2.62 V compared to the values of 0.40 and 0.48 V for fully –O and –OH models. Besides, charge density difference (CDD) plots in Fig. S11 of the ESI† reveal a lower electron accumulation on –F moieties compared to –O and –OH groups, implying that the former is less attractive towards H^+ reactants.

Further support to the –O termination role favouring the O-TER path is provided by the $F_{3/9}O_{4/9}OH_{2/9}$ model, where a –OH moiety is substituted by an –O one. From the previous reasoning, it should stabilize O-TER, and that is indeed what happens. In going from the $F_{1/3}O_{1/3}OH_{1/3}$ to the $F_{3/9}O_{4/9}OH_{2/9}$ model, O-TER gets stabilized by 0.45 eV to a final ΔG value of the Volmer step of solely 0.01 eV. On the other hand, the TER–TER path is no longer the preferred patch, since the Tafel step is more endergonic, by 0.21 eV up to a value of 0.29 eV, and the subsequent first Volmer step is 0.10 eV above the HER equilibrium, requiring a U of −0.10 V to make the full electrochemical steps exergonic. With respect to the OH-TER path, it still gets disfavoured, with an initial Heyrovsky step of 0.32 eV. In any case, the F-containing models are those that adjust best their U with the HER working conditions.

Having analysed the influence of mixed terminations on several HER mechanisms, one may wonder whether the standard Volmer–Tafel path could be competitive on such models. Fig. 6 shows that, for the fully O-terminated case, the binary and ternary models would require working at excessively low U overpotentials. The standard Volmer–Tafel path has not been considered for pristine Ti_3C_2 since it is excessively active, *vide supra*, whereas the fully F-terminated case has also been disregarded since it is excessively inactive (*cf.* Fig. 4). Also, the fully OH-terminated case has not been investigated because there is simply no room for Volmer steps and this is also the situation for the fully H-terminated case. Inspecting the profiles in Fig. 6, one realizes that PCET steps are exergonic in the fully O-terminated case, because of the strong affinity towards H. Note that this termination would be only stable at high U values, see Fig. 3. As per the binary and ternary cases, the Volmer steps are quite endergonic for $O_{1/3}OH_{2/3}$, $O_{1/2}OH_{1/2}$, and $F_{1/3}O_{1/3}OH_{1/3}$, with potential determining steps with U values of −0.74, −0.74, and −0.58 V, respectively. The $F_{3/9}O_{4/9}OH_{2/9}$ model is not so endergonic, but with a sensible U value of −0.46 V. Indeed, the only viable Volmer–Tafel mechanism is found in the case of $O_{2/3}OH_{1/3}$, with very low ΔG_H values for the two consecutive Volmer steps, and a U value of solely −0.09 V, competitive to the value of −0.01 V for the same model following the O-TER Volmer–Heyrovsky mechanism, but not preferred to this last one, though. Thus, except perhaps for the last commented possible competitive pathway, the standard Volmer–Tafel mechanism is not preferred in any of the explored models, but other sequencing of the mechanisms, like the TER–TER, are actually favourable in some models as already commented.

3.3. HER electrocatalysis performance

All in all, an optimal HER catalyst should have a very small ΔG_H, ideally going to 0, implying no overpotential. This is because an excessively low ΔG_H makes it difficult for H* adatoms to combine and form H_2, while excessively positive ΔG_H leads to slow HER kinetics.[76] In general, it is well accepted that a good HER activity would follow the classical rule of $|\Delta G_H| < 0.2$ eV,[77] adopted as well in discussing the present calculations. On the other hand, F-free models can also display very low U values, ranging from −0.01 to −0.23 V, while these overpotentials are either within or close to those where the stability regions of the considered models lie, meaning that these can be regarded as valid, in particular when accounting for the DFT inherent accuracy, *vide supra*.

Thus, having –F groups on the surface is not necessarily detrimental, and indeed helps understanding previous experimental observations,[73] in the sense that large –F coverages, approaching the full –F situation, make HER unpracticable. However, according to the present study, low coverages of –F moieties, like $F_{1/3}$, can further improve the HER process by reducing the $|\Delta G_H|$ constraint beyond that encountered in the F-free situations. This is probably due to subtle lateral interactions, and also helping to avoid having patches of only –O termination, which became excessively active towards H leading to a passivated surface. Aside from this, the observed increase of concentration of –O moieties is beneficial for the HER,[73] but up to a certain degree, *e.g.* $O_{2/3}$, since a fully O-terminated situation is too active towards hydrogen, plus actually not stable under working conditions according to the Pourbaix diagrams in Fig. 3.

With the previous reaction profiles, one can get estimates of the theoretical overpotential, $\eta = U_{RHE} - U$, at which the HER could be carried out. These are encompassed in Tables 1 and S1 of the ESI† for the most likely reaction mechanism, and the values represented in Fig. 7 on a typical volcano plot,[78] where the abscissa represents the ΔG_H descriptor while the ordinate represents the overpotential. Notice that values on the left and right branches of the volcano plot represent strong and weak H* adsorptions, respectively. In any case, one can readily observe that any Ti_3C_2 MXene with mixed termination groups feature better HER activity than those fully terminated, and that, in particular, F-free O-rich situations such as the one in the $O_{2/3}OH_{1/3}$ model, and F-containing situations as in the $F_{1/3}O_{1/3}OH_{1/3}$ and $F_{3/9}O_{4/9}OH_{2/9}$ models appear to be optimal for the HER, the latter being stable under the working conditions of applied potential, see Pourbaix diagrams in Fig. 3.

According to the previous discussion, some of the Ti_3C_2 terminated MXenes could be competitive or even better electrocatalysts for the HER when compared to other materials

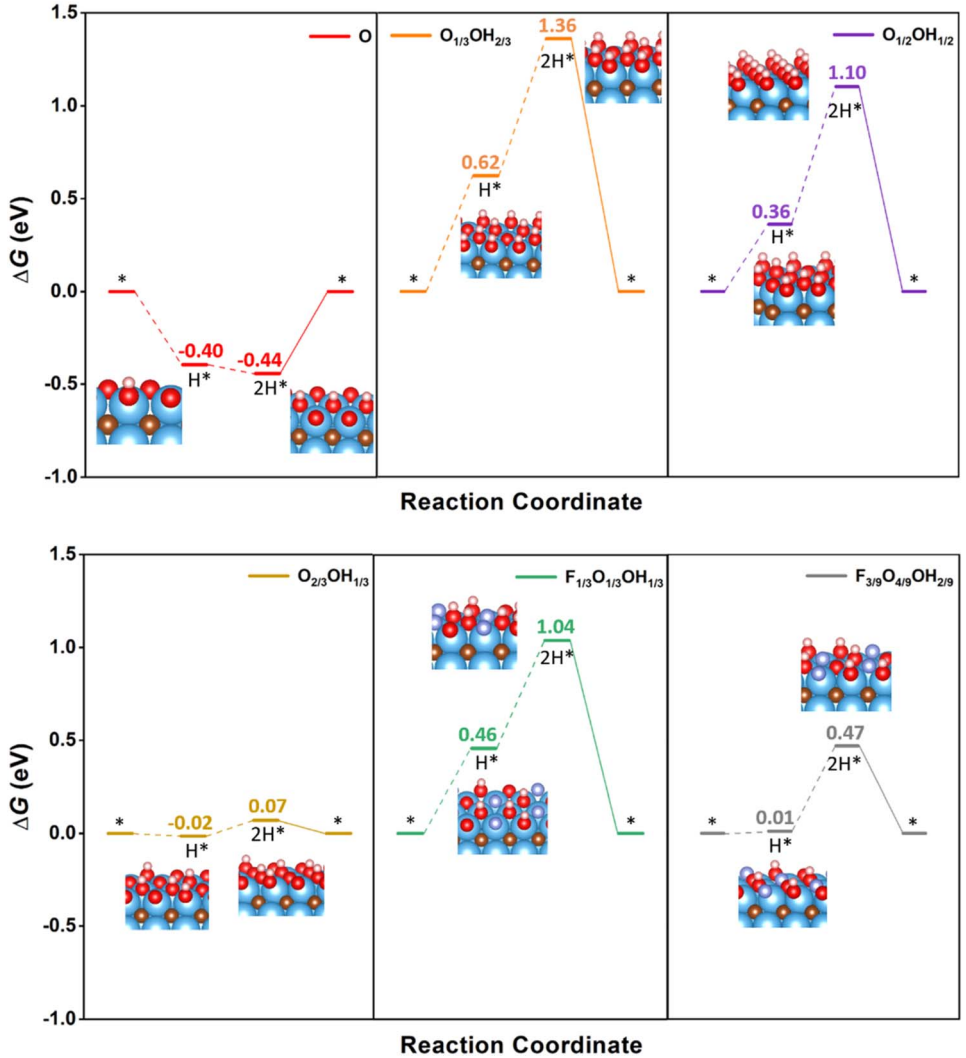

Fig. 6 Gibbs free energy, Δ*G*, diagram of the HER on selected binary and ternary terminations of the Ti_3C_2 (0001) surface combining –O, –OH, and –F moieties, under standard working conditions, following the standard Volmer–Tafel mechanism sequence. Solid lines represent the chemical step of the as-generated H_2 desorption, while dashed lines represent the electrochemical PCET steps. Color coding as in Fig. 4.

reported in the literature, estimated, *e.g.*, with similar DFT exchange–correlations and coverages, including Pt,[79] MoS_2,[80] WS_2,[81] graphitic carbonitride with N-doped graphene, *i.e.*, C_3N_4@NG,[82] and C_3N material,[83] to include just some of the most prominent ones. In particular, as stated above, situations corresponding to the $O_{2/3}OH_{1/3}$, $F_{1/3}O_{1/3}OH_{1/3}$, and $F_{3/9}O_{4/9}OH_{2/9}$ models appear to be the optimal cases, even if accounting for DFT inherent accuracy. Thus, proper surface terminated Ti_3C_2 MXenes emerge as a promising material for the HER, especially when accounting for their high surface area, abundance and lightness of the constituent elements, which fosters high performances per unit area or materials grams. Still, one should not consider these as definitive situations, but rather as indicative, since other stoichiometries and arrangements surely exist which are not regarded in the present study when constructing the Pourbaix diagrams, and also regarding the inherent accuracy of DFT. But, clearly, O-rich binary terminations admixing –O and –OH groups can be claimed as responsible for a good HER activity at low pH and F-free conditions, while ternary systems mixing –F, –O, and –OH groups are responsible for the same performance in F-containing situations.

Last but not least, one could attempt at understanding the main trends favoring the predicted HER mechanism. This is tackled here by calculating the Bader charges of the termination groups, as shown in Fig. 8. Let us consider first binary situations with different ratios of –O and –OH surface groups. As observed in Fig. 8, the negative net charge of –O groups increases with the –O ratio, and would reach a limit of $-1.09e$ for a fully O-terminated model. Inversely, the negative net charge of –OH groups decreases when the O concentration increases (or the OH one decreases), from an ideal value of $-0.73e$ for the fully OH-terminated case. Thus, the larger the net negative charge on –O moieties, the stronger the H^+ attraction and, consequently, the more stable the H* becomes. However, a suitable value of -0.01 eV is found for $O_{2/3}OH_{1/3}$, since fully O-terminated Ti_3C_2 attaches the H adatoms too strongly, with a ΔG_H of -0.40 eV, which is detrimental for the HER process.

Table 1 Summary of the potential determining steps, based on the calculated ΔG_H as a descriptor, on the explored Ti_3C_2 models, either pristine, or covered according to the specified terminations. The required overpotential, η, is specified, as well as the preferred Volmer–Heyrovsky (VH) or Volmer–Tafel (VT) mechanism, specifying the subtype of path, either O-TER, OH-TER, or TER–TER. In the case of pristine Ti_3C_2, note that the strong H-affinity prevents any H_2 formation, regardless of η

Model	Mechanism	Subtype	ΔG_H/eV	η/V
Pristine Ti_3C_2	—	—	−1.32	—
O	VH	—	−0.40	0.40
H	VH	—	0.63	0.63
OH	VH	—	−0.48	0.48
F	VH	—	2.62	2.62
$O_{1/3}OH_{2/3}$	VH	OH-TER	0.08	0.08
$O_{1/2}OH_{1/2}$	VH	OH-TER	0.23	0.23
$O_{2/3}OH_{1/3}$	VH	O-TER	−0.01	0.01
$F_{1/3}O_{1/3}OH_{1/3}$	VT	TER–TER	−0.01	0.01
$F_{3/9}O_{4/9}OH_{2/9}$	VH	O-TER	0.01	0.01

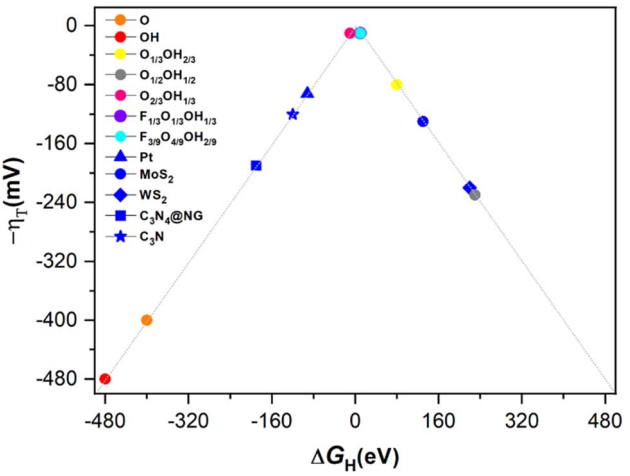

Fig. 7 Volcano plot of $-\eta$ *vs.* ΔG_H on the different terminated Ti_3C_2 surface models, including fully O- and OH-terminated cases, as well as binary situations represented by the $O_{1/3}OH_{2/3}$, $O_{1/2}OH_{1/2}$, and $O_{2/3}OH_{1/3}$ models, and ternary ones as in the $F_{1/3}O_{1/3}OH_{1/3}$ and $F_{3/9}O_{4/9}OH_{2/9}$ models. In addition, reference values for Pt, MoS_2, WS_2, C_3N_4@NG, and C_3N are included for comparison.

The observed trends in net charges of –OH and –O groups are maintained when having –F groups at the surface. For instance, the Bader charges of –O and –OH groups in the $F_{1/3}O_{1/3}OH_{1/3}$ model are -0.38 and $-0.22e$, respectively, similar to those found for the same ratios of -0.39 and $-0.22e$ on $O_{1/3}OH_{2/3}$ and $O_{2/3}OH_{1/3}$ models, respectively. Moreover, the net charge at –O of $-0.57e$ in $O_{1/2}OH_{1/2}$ is similar and follows the observed trend when compared to the $F_{3/9}O_{4/9}OH_{2/9}$ of $-0.50e$, and actually the –OH charge of $-0.14e$ follows the trend when decreasing the OH ratio. Finally, the –F net charge is maintained constant at $-0.26e$ for both $F_{1/3}O_{1/3}OH_{1/3}$ and $F_{3/9}O_{4/9}OH_{2/9}$, thus irrespective of the –O/–OH ratio. Thus, charges on a moiety are largely independent of the presence of other moieties, in line with the information obtained from CDD plots in Fig. S11 of the

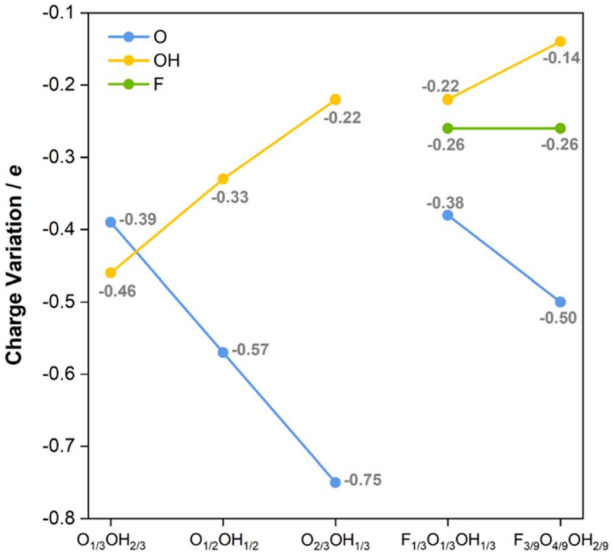

Fig. 8 Bader charges, in *e*, of –F, –O, and –OH groups on the diverse binary (admixing –O and –OH moieties) and ternary (admixing –F, –O, and –OH moieties).

ESI,† and solely affected by their surface concentration. Keeping this in mind, but also regarding the trend of ΔG_H with respect to the –O charge, one may wonder which is the origin of the small overpotentials on the F-containing models, when the charge on –O decreases. The answer seems to be related, on one hand, to the negative charge on –F groups, and, on the other hand, to the larger electronic affinity of –F. The resulting net generates a stronger attractive electric field towards the H^+ reactant, which may favor the adsorption, but in a more moderate fashion. This agrees with previous experimental results,[84,85] stating that the higher the featured –F coverage, the lower the HER activity on $Ti_3C_2T_x$, whereas compared to –O terminations, lower –F coverage promotes the H^+ adsorption and decreases the Gibbs free energy change of the HER.

4. Conclusions

In the present work we studied the potential HER performance of Ti_3C_2 MXene and, in particular, the effect of terminations by considering fully –O, –OH, –F, and –H terminations, as well as a pristine surface, but also mixed terminations, either binary or ternary, considering as well different ratios of surface moieties. To assess the most likely terminations under HER conditions of low pH and *U*, Pourbaix diagrams were built after examining the stability of *ca.* 450 different surface terminations, with variances in composition, species ratios, and topologically different arrangements. The cases with –F terminations were treated separately since there are synthetic procedures that do not use this element as the etchant. On top of that, different Volmer–Tafel and Volmer–Heyrovsky HER mechanisms were investigated on the obtained surface models, considering the initial or later involvement of surface H atoms from –H or –OH groups.

The reported results highlight that, at variance with a number of previous studies, fully –O, –OH, and –H

terminations are possible, but only at very positive (–O) or negative (–OH and –H) potentials with respect to the RHE reference. Interestingly, close to the HER equilibrium conditions, binary models admixing –O and –OH moieties are predicted to be preferred for F-free situations, while ternary models also containing –F are relevant in F-containing samples. In particular, based on the $O_{2/3}OH_{1/3}$ and $F_{3/9}O_{4/9}OH_{2/9}$ models using –O moieties as the active center the Volmer–Heyrovsky mechanism is found to be optimal with almost negligible overpotential. For a lower –F content, as in the $F_{1/3}O_{1/3}OH_{1/3}$ model, a Volmer–Tafel like mechanism, where a Tafel step is initially carried out involving surface –OH groups, followed by two Volmer steps to regenerate the electrocatalysts as-generated –O centers, is also found to be optimal featuring an almost inexistent overpotential of 0.01 V. These two situations appear to be quite competitive when compared to other electrocatalysts used for the HER in the literature, such as Pt, MoS_2, or WS_2.

The analysis of electronic structure and charge density reveals that larger the concentration of –O moieties on the Ti_3C_2 surface, the more negatively charged they become with a concomitant stronger ability for H^+ reduction, reaching moderate bond strengths when the –O coverage is $\frac{2}{3}$. The presence of –F groups is not detrimental *per se*, and actually, their negative charge and the stronger electric field they generate contribute to favoring the H^+ reduction with moderate adsorption strength even when having a lower –O coverage of *ca.* $\frac{1}{3}$, as in the $F_{3/9}O_{4/9}OH_{2/9}$ and $F_{1/3}O_{1/3}OH_{1/3}$ models, which explains and reconciles previous experimental reports pointing out to better performances when having a higher presence of –O groups, and a lower presence of –F ones.[73] Finally, the present study underscores the tunability of these surface terminations to maximize the HER performance, while addressing their stability under working conditions of pH and *U*.

Conflicts of interest

There are no conflicts of interest to declare.

Acknowledgements

The research carried out at the Universitat de Barcelona has been supported by the Spanish MCIN/AEI/10.13039/501100011033 PID2021-126076NB-I00 project, funded partially by FEDER Una manera de hacer Europa, and María de Maeztu CEX2021-001202-M grants, including funding from the European Union and, in part, by COST Action CA18234. A significant part of the computational resources has been provided by the Red Española de Supercomputación (RES) QHS-2022-1-0004 and QHS-2021-3-0012. L. M. thanks the HPC-EUROPA3 (HPC17OOIBY) project supported by the EC Research Innovation Action under the H2020 Programme. L. M. thanks the China Scholarship Council (CSC) for financing her PhD (CSC202108390032).

References

1 M. Dresselhaus and I. Thomas, *Nature*, 2001, **414**, 332–337.
2 J. A. Turner, *Science*, 2004, **305**, 972–974.
3 S. Chu and A. Majumdar, *Nature*, 2012, **488**, 294–303.
4 S. E. Hosseini and M. A. Wahid, *Renewable Sustainable Energy Rev.*, 2016, **57**, 850–866.
5 J. Greeley, T. F. Jaramillo, J. Bonde, I. Chorkendorff and J. K. Nørskov, *Nat. Mater.*, 2006, **5**, 909–913.
6 X. X. Zou and Y. Zhang, *Chem. Soc. Rev.*, 2015, **44**, 5148–5180.
7 J. N. Hansen, H. Prats, K. K. Toudahl, N. M. Secher, K. Chan, J. Kibsgaard and I. Chorkendorff, *ACS Energy Lett.*, 2021, **6**, 1175–1180.
8 D. E. Brown, M. N. Mahmood, M. C. M. Man and A. K. Turner, *Electrochim. Acta*, 1984, **29**, 1551–1556.
9 I. A. Raj and K. I. Vasu, *J. Appl. Electrochem.*, 1990, **20**, 32–38.
10 M. A. Lukowski, A. S. Daniel, F. Meng, A. Forticaux, L. Li and S. Jin, *J. Am. Chem. Soc.*, 2013, **135**, 10274–10277.
11 T. F. Jaramillo, K. P. Jørgensen, J. Bonde, J. H. Nielsen, S. Horch and I. Chorkendorff, *Science*, 2007, **317**, 100–102.
12 G. Gao, Y. Jiao, F. Ma, Y. Jiao, E. Waclawik and A. Du, *J. Phys. Chem. C*, 2015, **119**, 13124–13128.
13 J. Kibsgaard, C. Tsai, K. Chan, J. D. Benck, J. K. Nørskov, F. Abild-Pedersen and T. F. Jaramillo, *Energy Environ. Sci.*, 2015, **8**, 3022–3029.
14 Y. Zheng, Y. Jiao, J. Chen, J. Liu, J. Liang, A. Du, W. Zhang, Z. Zhu, S. C. Smith, M. Jaroniec, G. Q. Lu and S. Z. Qiao, *J. Am. Chem. Soc.*, 2011, **133**, 20116–20119.
15 G. Gao, Y. Jiao, F. Ma, Y. Jiao, E. Waclawik and A. Du, *J. Catal.*, 2015, **332**, 149–155.
16 G. Gao, Y. Jiao, F. Ma, Y. Jiao, E. Waclawik and A. Du, *Phys. Chem. Chem. Phys.*, 2015, **17**, 31140–31144.
17 H. Fei, J. Dong, M. J. Arellano-Jiménez, G. Ye, N. Dong Kim, E. L. G. Samuel, Z. Peng, Z. Zhu, F. Qin, J. Bao, M. J. Yacaman, P. M. Ajayan, D. Chen and J. Tour, *Nat. Commun.*, 2015, **6**, 8668.
18 G. P. Gao, A. P. O'Mullane and A. J. Du, *ACS Catal.*, 2017, **7**, 494–500.
19 B. Anasori, M. R. Lukatskaya and Y. Gogotsi, *Nat. Rev. Mater.*, 2017, **2**, 16098.
20 M. Naguib, M. Kurtoglu, V. Presser, J. Lu, J. Niu, M. Heon, L. Hultman, Y. Gogotsi and M. W. Barsoum, *Adv. Mater.*, 2011, **23**, 4248–4253.
21 M. Ghidiu, M. R. Lukatskaya, M. Q. Zhao, Y. Gogotsi and M. W. Barsoum, *Nature*, 2014, **516**, 78–81.
22 X. Yu, X. Cai, H. Cui, S. W. Lee, X. F. Yu and B. Liu, *Nanoscale*, 2017, **9**, 17859–17864.
23 V. Kamysbayev, A. S. Filatov, H. Hu, X. Rui, F. Lagunas, D. Wang, R. Klie and D. V. Talapin, *Science*, 2020, **369**, 979–983.
24 I. Persson, J. Halim, H. Lind, T. W. Hansen, J. B. Wagner, L.-Å. Näslund, V. Darakchieva, J. Palisaitis, J. Rosen and P. O. Å. Persson, *Adv. Mater.*, 2019, **31**, 1805472.
25 X. Sang, Y. Xie, M.-W. Lin, M. Alhabeb, K. L. Van Aken, Y. Gogotsi, P. R. C. Kent, K. Xiao and R. R. Unocic, *ACS Nano*, 2016, **10**, 9193–9200.
26 J. Xie, X. Yang and Y. Xie, *Nanoscale*, 2020, **12**, 4283–4294.
27 R. He, Y. Wan, P. Zhao, P. Guo, Z. Jiang and J. Zheng, *Comput. Theor. Chem.*, 2019, **1150**, 26–39.

28 J. Peng, X. Chen, W. J. Ong, X. Zhao and N. Li, *Chem*, 2019, **5**, 18–50.
29 J. Ran, G. Gao, F. T. Li, T. Y. Ma, A. Du and S. Z. Qiao, *Nat. Commun.*, 2017, **8**, 13907.
30 C. Ling, L. Shi, Y. Ouyang and J. Wang, *Chem. Mater.*, 2016, **28**, 9026–9032.
31 Z. W. Seh, K. D. Fredrickson, B. Anasori, J. Kibsgaard, A. L. Strickler, M. R. Lukatskaya, Y. Gogotsi, T. F. Jaramillo and A. Vojvodic, *ACS Energy Lett.*, 2016, **1**, 589–594.
32 H. Pan, *Sci. Rep.*, 2016, **6**, 32531.
33 J. Xie, J. Qi, F. Lei and Y. Xie, *Chem. Commun.*, 2020, **56**, 11910–11930.
34 J. Xie and Y. Xie, *ChemCatChem*, 2015, **7**, 2568–2580.
35 M. A. Hope, A. C. Forse, K. J. Griffith, M. R. Lukatskaya, M. Ghidiu, Y. Gogotsi and C. P. Grey, *Phys. Chem. Chem. Phys.*, 2016, **18**, 5099–5102.
36 R. Ibragimova, M. J. Puska and H.-P. Komsa, *ACS Nano*, 2019, **13**, 9171–9181.
37 M. López, Á. Morales-García, F. Viñes and F. Illas, *ACS Catal.*, 2021, **11**, 12850–12857.
38 J. D. Gouveia, Á. Morales-García, F. Viñes, F. Illas and J. R. B. Gomes, *Appl. Catal., B*, 2020, **260**, 118191.
39 J. Durst, A. Siebel, C. Simon, F. Hasché, J. Herranz and H. A. Gasteiger, *Energy Environ. Sci.*, 2014, **7**, 2255–2260.
40 P. J. Rheinländer, J. Herranz, J. Durst and H. A. Gasteiger, *J. Electrochem. Soc.*, 2014, **161**, F1448.
41 S. Li, P. Tuo, J. Xie, X. Zhang, J. Xu, J. Bao, B. Pan and Y. Xie, *Nano Energy*, 2018, **47**, 512–518.
42 C. Liu, H. Wu, X. Wang, J. Fan, H. Su, D. Yang, Y. Wei, F. Du, Y. Dall'Agnese and Y. Gao, *Energy Storage Mater.*, 2023, **54**, 164–171.
43 H. Xu, J. Fan, H. Su, C. Liu, G. Chen, Y. Dall'Agnese and Y. Gao, *Nano Lett.*, 2023, **23**, 283–290.
44 S. Ma, X. L. Fan, Y. R. An, D. X. Yang, Z. F. Luo, Y. Hu and N. J. Guo, *J. Mater. Sci.*, 2019, **54**, 11378–11389.
45 H. C. Yang, Y. D. Ma, X. S. Lv, B. B. Huang and Y. Dai, *J. Catal.*, 2020, **387**, 12–16.
46 N. Li, Z. L. Zeng, Y. W. Zhang, X. Z. Chen, Z. Z. Kong, Arramel, Y. Li, P. Zhang and B. S. Nguyen, *ACS Omega*, 2021, **6**, 23676–23682.
47 G. Kresse and J. Furthmüller, *Phys. Rev. B: Condens. Matter Mater. Phys.*, 1996, **54**, 11169.
48 G. Kresse and D. Joubert, *Phys. Rev. B: Condens. Matter Mater. Phys.*, 1999, **59**, 1758.
49 J. P. Perdew, K. Burke and M. Ernzerhof, *Phys. Rev. Lett.*, 1996, **77**, 3865.
50 H. J. Monkhorst and J. D. Pack, *Phys. Rev. B: Solid State*, 1976, **13**, 5188.
51 S. Grimme, J. Antony, S. Ehrlich and H. Krieg, *J. Chem. Phys.*, 2010, **132**, 154104.
52 R. Morales-Salvador, J. D. Gouveia, Á. Morales-García, F. Viñes, J. R. B. Gomes and F. Illas, *ACS Catal.*, 2021, **11**, 11248–11255.
53 B. E. Conway and B. V. Tilak, *Electrochim. Acta*, 2002, **47**, 3571–3594.
54 X. Huang, J. Wang, H. B. Tao, H. Tian, Z. Zhang and H. Xu, *J. Catal.*, 2020, **389**, 461–467.
55 J. N. Brønsted, *Chem. Rev.*, 1928, **5**, 231–338.
56 M. G. Evans and M. Polanyi, *Trans. Faraday Soc.*, 1938, **34**, 11–24.
57 K. S. Exner, J. Anton, T. Jacob and H. Over, *Angew. Chem., Int. Ed.*, 2016, **55**, 7501–7504.
58 K. S. Exner and H. Over, *Acc. Chem. Res.*, 2017, **50**, 1240–1247.
59 J. K. Nørskov, J. Rossmeisl, A. Logadottir, L. Lindqvist, J. R. Kitchin, T. Bligaard and H. Jónsson, *J. Phys. Chem. B*, 2004, **108**, 17886–17892.
60 *NIST Standard Reference Database*, SRD Number 69, 1901, DOI: 10.18434/T4D303.
61 Q. Li, Y. Ouyang, S. Lu, X. Bai, Y. Zhang, L. Shi, C. Ling and J. Wang, *Chem. Commun.*, 2020, **56**, 9937–9949.
62 M. Pourbaix, *Atlas of Electrochemical Equilibria in Aqueous Solutions*, National Association of Corrosion Engineers (NACE), Houston, Texas, USA, 1974.
63 M. López, K. S. Exner, F. Viñes and F. Illas, *Adv. Theory Simul.*, 2022, 2200217.
64 D. F. Sriver and P. W. Atkins, *Inorganic Chemistry*, Freeman, W.H. and Company, New York, 5th edn, 2009.
65 D. R. Lide, *CRC Handbook of Chemistry and Physics*, CRC Press, Boca Raton, Florida, 102nd edn, 2004.
66 H. A. Hansen, I. C. Man, F. Studt, F. Abild-Pedersen, T. Bligaard and J. Rossmeisl, *Phys. Chem. Chem. Phys.*, 2010, **12**, 283–290.
67 N. Xue, X. Li, L. Han, H. Zhu, X. Zhao, J. Zhuang, Z. Ga and X. Tao, *J. Mater. Chem. A*, 2022, **10**, 7960–7967.
68 S. Yang, P. Zhang, F. Wang, A. G. Ricciardulli, M. R. Lohe, P. W. M. Blom and X. Feng, *Angew. Chem., Int. Ed.*, 2018, **19**, 15717–15721.
69 S.-Y. Pang, Y.-T. Wong, S. Yuan, Y. Liu, M.-K. Tsang, Z. Yang, H. Huang, W.-T. Wong and J. Hao, *J. Am. Chem. Soc.*, 2019, **141**, 9610–9616.
70 J. Gan, F. Li, Y. Tang and Q. Tang, *ChemSusChem*, 2020, **13**, 6005–6015.
71 Y. Jiang, T. Sun, X. Xie, W. Jiang, J. Li, B. Tian and C. Su, *ChemSusChem*, 2019, **12**, 1368–1373.
72 C. Ling, L. Shi, Y. Ouyang and J. Wang, *Chem. Mater.*, 2016, **28**, 9026–9032.
73 A. D. Handoko, H. T. Chen, Y. W. Lum, Q. F. Zhang, B. Anasori and Z. W. She, *iScience*, 2020, **23**, 101181.
74 F. Viñes, C. Sousa, P. Liu, J. A. Rodriguez and F. Illas, *J. Chem. Phys.*, 2005, **122**, 174709.
75 M. Khazaei, M. Arai, T. Sasaki, C. Y. Chung, N. S. Venkataramanan, M. Estili, Y. Sakka and Y. Kawazoe, *Adv. Funct. Mater.*, 2013, **23**, 2185–2192.
76 G. P. Gao, A. P. O'Mullane and A. J. Du, *ACS Catal.*, 2017, **7**, 494–500.
77 B. Huang, N. G. Zhou, X. Z. Chen, W. J. Ong and N. Li, *Chem.–Eur. J.*, 2018, **24**, 18479–18486.
78 N. Li, Z. L. Zeng, Y. W. Zhang, X. Z. Chen, Z. Z. Kong, Arramel, Y. Li, P. Zhang and B. S. Nguyen, *ACS Omega*, 2021, **6**, 23676–23682.
79 J. K. Nørskov, T. Bligaard, A. Logadottir, J. Kitchin, J. G. Chen, S. Pandelov and U. Stimming, *J. Electrochem. Soc.*, 2005, **152**, J23–J26.

80 L. Lin, N. Miao, Y. Wen, S. Zhang, P. Ghosez, Z. Sun and D. A. Allwood, *ACS Nano*, 2016, **10**, 8929–8937.
81 J. Bonde, P. G. Moses, T. F. Jaramillo, J. K. Nørskov and I. Chorkendorff, *Faraday Discuss.*, 2009, **140**, 219–231.
82 Y. Zheng, Y. Jiao, Y. Zhu, L. H. Li, Y. Han, Y. Chen, A. Du, M. Jaroniec and S. Z. Qiao, *Nat. Commun.*, 2014, **5**, 3783.
83 S. Yao, X. Zhang, A. Chen, Z. Zhang, M. Jiao and Z. Zhou, *J. Mater. Chem. A*, 2019, **7**, 19290–19296.
84 A. D. Handoko, K. D. Fredrickson, B. Anasori, K. W. Convey, L. R. Johnson, Y. Gogotsi, A. Vojvodic and Z. W. Seh, *ACS Appl. Energy Mater.*, 2018, **1**, 173–180.
85 Y. Zhang, L. Chen, Y. Gui and L. Liu, *Appl. Surf. Sci.*, 2022, **592**, 153334.